Hindawi
Journal of Nanomaterials
Volume 2024, Article ID 9577778, 9 pages
https://doi.org/10.1155/2024/9577778

Research Article

Crystallographic, Morphological, Magnetic, and Thermal Characterization of Superparamagnetic Magnetite Nanoparticles (Fe_3O_4) Synthesized by Chemical Coprecipitation Method and Calcined at 250°C for 4 hr

Md. Abdus Sabur and Md. Abdul Gafur

Pilot Plant and Process Development Centre, Bangladesh Council of Scientific and Industrial Research (BCSIR), Dhanmondi, Dhaka 1205, Bangladesh

Correspondence should be addressed to Md. Abdus Sabur; sabur37971@gmail.com

Received 16 October 2023; Revised 27 December 2023; Accepted 8 January 2024; Published 22 January 2024

Academic Editor: Xiaoqian Wang

Magnetite nanoparticles (Fe_3O_4) were prepared by chemical coprecipitation method using ferric chloride ($FeCl_3$) and heptahydrate ferrous sulfate ($FeSO_4{\cdot}7H_2O$) salts employing sodium hydroxide (NaOH) as a precipitant. To determine the size, shape, and chemical makeup of the produced magnetite nanoparticles, the generated powders were examined by transmission electron microscope, scanning electron microscope, atomic force microscope, and X-ray diffractometer. It was found that the magnetite powder had made a face-centered cubic crystal structure and spherical-like particle form with particle diameters of about 30 nm. The magnetic properties of magnetite nanoparticles were evaluated using a vibrating sample magnetometer. The obtained superparamagnetic properties of the produced nanoparticles, with saturation magnetization and coercivity of 50.75 emu/g and 30.09 Oe, respectively, allow them for applications in drug delivery, MRI contrast agent, catalysis, degradation of antibiotics, antibacterial activity, removal of heavy metals and organic dyes, etc.

1. Introduction

Applications involving iron oxide nanoparticles (IONPs) are receiving a lot of interest in industries that need a lot of them, like agriculture and biomass recovery [1–3] and wastewater treatment [4]. Higher quality requirements for IONPs lead to their use in catalysis [5], batteries [6], and particularly in biomedicine [7–9], where they are used for drug delivery [10], cancer treatment using magnetic hyperthermia [11, 12], and as a contrast agent for MRI [13, 14].

The oxide phase, particle shape, size and size distribution, internal composition (such as impurities and grain boundaries), and surface chemistry all have a significant impact on how well they work. Therefore, each application needs a customized synthetic process that can consistently produce the needed IONPs in amounts greater than the lab scale. The numerous investigations on IONP syntheses [9, 14–16] demonstrate that there is still much to learn about the development of such scalable synthesis and, consequently, large-scale production.

Highly monodisperse IONPs of tunable size can be produced utilizing techniques that thermally decompose precursors as ferric acetylacetonates in high-boiling-point organic solvents [17–19], and instances of scalable synthesis are known to exist [20]. An in-depth understanding of the particle generation mechanism during thermal decomposition syntheses was achieved because of the relatively long reaction times (of the order of an hour) that allow for thorough examination during the synthesis [21–23]. However, because these syntheses require high temperatures (often > 250°C) and expensive chemicals, they are labor and resource-intensive (particularly for large-scale manufacturing). In addition, if IONPs need to be disseminated in aqueous solutions, thermal decomposition syntheses necessitate postprocessing processes, such as purification and phase transfer, typically after a time-consuming

ligand exchange step. This is true for the majority of biological applications, where the regularly employed compounds for thermal breakdown also face significant difficulties due to strict regulatory oversight. Water-based syntheses are, therefore, preferred. This is one of the reasons that the coprecipitation of iron salts in aqueous solutions, or the simultaneous precipitation of ferrous and ferric ions started by the addition of a base, is the most widely used method for synthesizing IONPs. The availability of inexpensive chemicals and straightforward experimental techniques at moderate temperatures (100°C) without harmful byproducts are further factors contributing to the success of coprecipitation synthesis.

The benefit of the coprecipitation method is that it gives a crystallite size in the small range contrasted with other synthesis processes based on the precipitating agent selected during the reaction. Likewise, the crystallite size and morphology of the material produced utilizing this technique can be controlled using capping agents. Higher yield, high product purity, the lack of necessity to use organic solvents, easily reproducible, and low cost are some of the common advantages of this method [24, 25]. However, the properties of the produced particles, such as size, shape, and composition, are highly dependent on the reaction parameters such as temperature, pH, ionic strength, nature of the basic solution, and so on.

Due to variability in IONP core sizes and the existence of agglomerates, coprecipitation syntheses are known to produce particles with a high polydispersity and a relatively low magnetism [16]. The stability and use of the IONPs are now complicated by these agglomerates. The simultaneous nucleation and development of particles, as well as the existence of intermediary phases before or during the production of the desirable magnetic phases, such as magnetite (Fe_3O_4) or maghemite (γ-Fe_2O_3), are likely to cause variations in core size [26, 27]. According to the synthesis circumstances (precursors utilized and their concentration, temperature, pH, order of reagent and stabilizer addition, etc.), the particle formation mechanism is still up for debate and is predicted to vary [28, 29].

In this study, sodium hydroxide (NaOH) was used as a precipitating agent together with ferric and ferrous salts to create magnetite nanoparticles. The nanoparticles were then analyzed using X-ray diffractometer (XRD), scanning electron microscope (SEM), transmission electron microscope (TEM), atomic force microscope (AFM), vibrating sample magnetometer (VSM), and thermal analysis (TG-DTA) to study the crystallographic, morphological, magnetic, and thermal properties of superparamagnetic magnetite nanoparticles.

2. Experimental Details

2.1. Materials. All of the chemical reagents utilized during the synthesis were analytical grade and did not require any additional purification. Anhydrous ferric chloride ($FeCl_3$), ferrous sulfate heptahydrate ($FeSO_4{\cdot}7H_2O$), and sodium hydroxide (NaOH) were purchased from Merck (India) with a purity ≥98%.

2.2. Synthesis of Magnetite Nanoparticles. Using the coprecipitation approach, magnetite nanoparticles (Fe_3O_4) were produced by mixing 100 ml 0.4 M $FeCl_3$ with 100 ml 0.2 M $FeSO_4{\cdot}7H_2O$ as a precursor. The ions Fe^{3+} and Fe^{2+} are created when the $FeCl_3$ solution and $FeSO_4$ solution react. As a precipitating agent, a 3 M solution of NaOH was added drop-by-drop to the salt solutions while being stirred continuously until the pH reached 12 and heated the solution at 80°C for 60 min. Then, with the help of a magnetic stirrer hot plate and a molar ratio of 2 : 1, Fe^{3+} and Fe^{2+} react with NaOH solution to produce coal-black Fe_3O_4 particles as a precipitate. After that, the material was continuously rinsed in distilled water until it achieved a pH level of 7 to obtain the pure Fe_3O_4 nanoparticles. Finally, particles were calcined for 4 hr at 250°C.

2.3. Characterization Techniques

2.3.1. XRD. The crystallographic properties of Fe_3O_4 were identified by recording *X*-ray powder diffraction patterns (XRD) of powder samples using a Rigaku Smart Lab SE *X*-ray Diffractometer equipped with a CuKα radiation source ($\lambda = 1.5406$ Å). Analysis was carried out at 25°C, 40 kV, and 50 mA. The 2θ measured range was 20°–70°, at 0.01° steps, with a scan speed of 25.00°/min.

2.3.2. SEM. The morphology of Fe_3O_4 nanoparticles was observed using the JEOLUSER 7610F SEM, which operated at 10 kV. SEM images were analyzed with ImageJ software to calculate the particle size distribution of the dried nanoparticles.

2.3.3. TEM. The morphology of the Fe_3O_4 nanoparticles was analyzed by TEM using a high-resolution LIBRA 120 Plus Carl Zeiss microscope. TEM images were analyzed with ImageJ software to calculate the particle size distribution of the dried nanoparticles.

2.3.4. AFM. AFM images were performed by CSI AFM nanoobserver microscopy in an oscillating mode using silicon cantilevers with a typical resonant frequency of 138.228 kHz, scanning speed of 750 mIn/s, resolution of 512×512, and scan size of $5 \times 5\,\mu$m. The AFM data were analyzed using the Gwyddion software.

2.3.5. VSM. The magnetic properties of Fe_3O_4 nanoparticles were measured using VSM in the quantum design physical property measurement system DYNACOOL at room temperature with a magnetic field in the range of −15,000 to 15,000 Oe. About 12.3 mg of dried samples were used for these measurements.

2.3.6. TG-DTA. The thermogravimetric and differential thermal analysis TG-DTA curves of Fe_3O_4 nanoparticles were obtained from EXSTAR 6000, TG/DTA 6300 thermal analyzer with a heating rate of 20°C/min. The mass of the solid specimen was about 15.032 mg and the whole measurements were carried out in a nitrogen atmosphere.

3. Result and Discussion

3.1. XRD Analysis. The XRD pattern of Fe_3O_4 nanoparticles is shown in Figure 1. This pattern is used to determine the crystal structure, lattice parameter, crystallite size, and crystal defects of Fe_3O_4 nanoparticles. In the XRD patterns, the

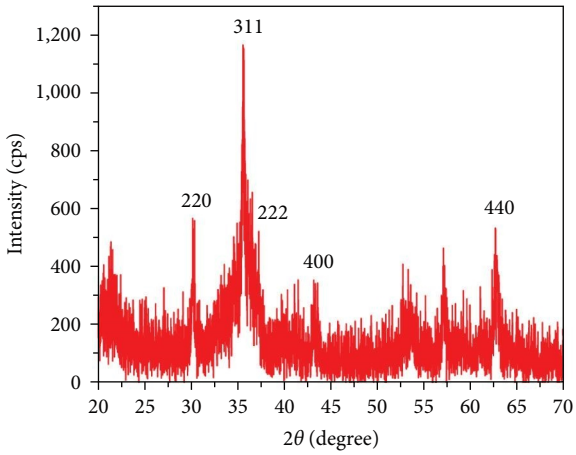

FIGURE 1: XRD pattern of Fe_3O_4 nanoparticles.

most intense XRD peak appears at $2\theta = 35.65°$, representing the (311) plane of Fe_3O_4 nanoparticles. Fe_3O_4 nanoparticles show strong peaks at $2\theta = 30.25$, 35.65, 36.37, 43.15, and 62.78, respectively, confirming the existence of diffraction planes for magnetite at 220, 311, 222, 400, and 440. These peaks have a cubic form and a crystalline structure that are typical of magnetite. As a result, the diffractogram of Fe_3O_4 nanoparticles meets the magnetite standard JCPDS 65-3107 (magnetite) requirements [30, 31].

The lattice parameter of the cubic crystal system is determined using the following formula:

$$a^2 = \frac{h^2 + k^2 + l^2}{d^2}, \quad (1)$$

where a is the lattice parameter, h, k, and l are the Miller indices, and d is the interplanar spacing. The calculated average lattice parameter of Fe_3O_4 nanoparticles is 8.398 Å (Table 1).

The crystallite size is calculated using Debye–Scherrer's formula given below:

$$D = \frac{K\lambda}{\beta \cos\theta}, \quad (2)$$

where D is the average size of the crystallite, λ is the wavelength of X-ray radiation, β is the full peak width at half-maximum (FWHM), and θ is the angle of diffraction. The average crystallite size of Fe_3O_4 nanoparticles is 17.698 nm [32], and 34.862 nm for the most intense peak (Table 1).

The number of dislocations in a unit volume of crystalline materials is determined according to the Segal method as follows:

$$\delta = \frac{1}{D^2}, \quad (3)$$

where δ is the dislocation density, and D is the crystallite size. The calculated average dislocation density of Fe_3O_4 nanoparticles is 3.219×10^{16} line/m^2 (Table 1).

The microstrain of a crystalline solid is calculated using the following formula:

$$\epsilon = \frac{\beta}{4\tan\theta}, \quad (4)$$

where ϵ is the microstrain of the crystal, β is the FWHM, and θ is the angle of diffraction. The average microstrain of Fe_3O_4 nanoparticles is found to be 0.0133 ppm (Table 1).

The crystallite size of Fe_3O_4 nanoparticles has a significant impact on their magnetic characteristics, such as the M_s, M_r, and H_c. Regardless of the shape and crystal structure of the particles, the M_s, M_r, and H_c rise with increasing crystallite size up to the critical limit [33]. The XRD data suggested that due to smaller crystallite size, the Fe_3O_4 nanoparticles are superparamagnetic as well as have smaller M_s and H_c.

3.2. SEM/EDAX Analysis. SEM images are used to examine the surface detail, shape, and average size of the synthesized Fe_3O_4 nanoparticles. Figure 2(a) displays an FESEM image of Fe_3O_4 nanoparticles. The SEM image of the synthesized Fe_3O_4 nanoparticles shows that they have a rough surface and a cavity-like structure. The average particle size of Fe_3O_4 nanoparticles is about 63 nm, which is determined using ImageJ software [34]. The histogram (Figure 2(b)) displays the size distribution of the nanoparticles, where the average diameter of the synthesized nanoparticles is determined to be 63.19 ± 7.12 nm. The EDAX spectrum of Fe_3O_4 nanoparticles reveals the presence of iron and oxygen (Figure 2(c)).

3.3. TEM Analysis. The TEM images are taken to determine the morphology, shape, and size of the Fe_3O_4 nanoparticles. Figure 3(a) illustrates the TEM image of Fe_3O_4 nanoparticles that were calcined at 250°C. The HR-TEM image (Figure 3(b)) displays tiny aggregated particles with a mean diameter of about 30 nm that are resolved using ImageJ software [34]. The histogram (Figure 3(c)) displays the size distribution of the nanoparticles, where the average diameter of the produced nanoparticles is determined to be 29.56 ± 7.9 nm. The majority of the nanoparticles have a size distribution between 25 and 35 nm. The selective area electron diffraction (SAED) pattern of Fe_3O_4 nanoparticles demonstrates the presence of concentric rings connected to several diffraction planes, indicating that produced Fe_3O_4 nanoparticles are polycrystalline (Figure 3(d)).

3.4. AFM Analysis. The morphology and the average size of Fe_3O_4 nanoparticles are evaluated by AFM. Before the microscopy analyses, one to two droplets of 0.1 mg/ml nanoparticles were deposited on a mica surface and left to dry at room temperature. Topography, amplitude, and phase contrast images from different regions over the sample surface are obtained and analyzed using the Gwyddion software [35]; some representative micrographs are shown in Figure 4(a)–4(c), respectively. Typical AFM images of magnetic nanoparticles (Figure 4) suggest that nanoparticles have a nearly spherical shape with an average diameter of 51.93 nm as well as have a single phase of Fe_3O_4 nanoparticles. Particle

Table 1: Crystallographic properties of Fe_3O_4 nanoparticles.

S. no.	2θ (°)	$h\ k\ l$	d (Å)	Lattice parameter (Å)	Crystallite size (nm)	Dislocation density (line/m^2)	Microstrain (ppm)
1	30.25	220	2.952	8.349	19.534	2.620×10^{15}	0.0071
2	35.65	311	2.516	8.344	34.862	8.227×10^{14}	0.0033
3	36.37	222	2.468	8.549	2.599	1.480×10^{17}	0.0446
4	43.15	400	2.095	8.380	12.057	6.878×10^{15}	0.0081
5	62.78	440	1.479	8.366	19.439	2.646×10^{15}	0.0035
Average				8.398	17.698	3.219×10^{16}	0.0133

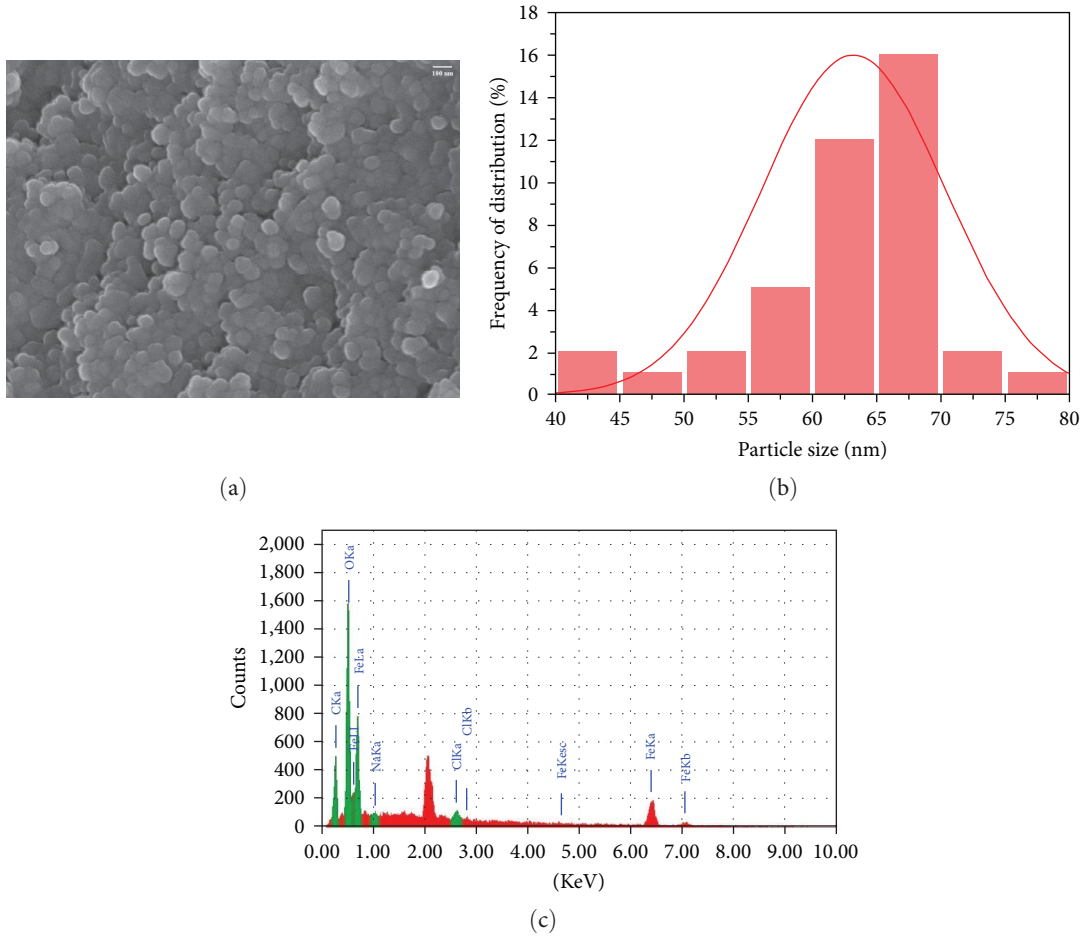

Figure 2: (a) FESEM image of Fe_3O_4 nanoparticles, (b) size distribution of Fe_3O_4 nanoparticles, and (c) EDAX image of Fe_3O_4 nanoparticles.

size and surface roughness of Fe_3O_4 nanoparticles are shown in Table 2.

3.5. VSM Analysis. The magnetic characteristics of Fe_3O_4 nanoparticles are evaluated using a VSM. Figure 5 shows the hysteresis loops of the Fe_3O_4 nanoparticles recorded at room temperature, and Table 3 lists the values for the magnetic properties. The magnetization curve for the synthesized magnetite nanoparticles described in this study demonstrates minimal values of remnant magnetization and coercivity field as well as very little hysteresis behavior for the samples. This demonstrates that superparamagnetic characteristics are present in the produced particles at normal temperatures. This is because when magnetite nanoparticles are smaller than the critical size of the magnetic domain size, they exhibit superparamagnetic characteristics [36–38]. The superparamagnetism and saturation magnetization (M_s) values in the nanosized magnetite samples are lower than the bulk magnetite value of 92 emu/g [39]. The saturated magnetization value of Fe_3O_4 nanoparticles is 50.75 emu/g. The decrease in saturation magnetization with smaller magnetite particle sizes has been explained in several ways. One aspect has to do with the spin disorder layer, which grows as crystallite size decreases. The result of a dipolar interaction between magnetite nanoparticles can also be used to explain another explanation for the decrease in the magnetic moment. The uneven shape of

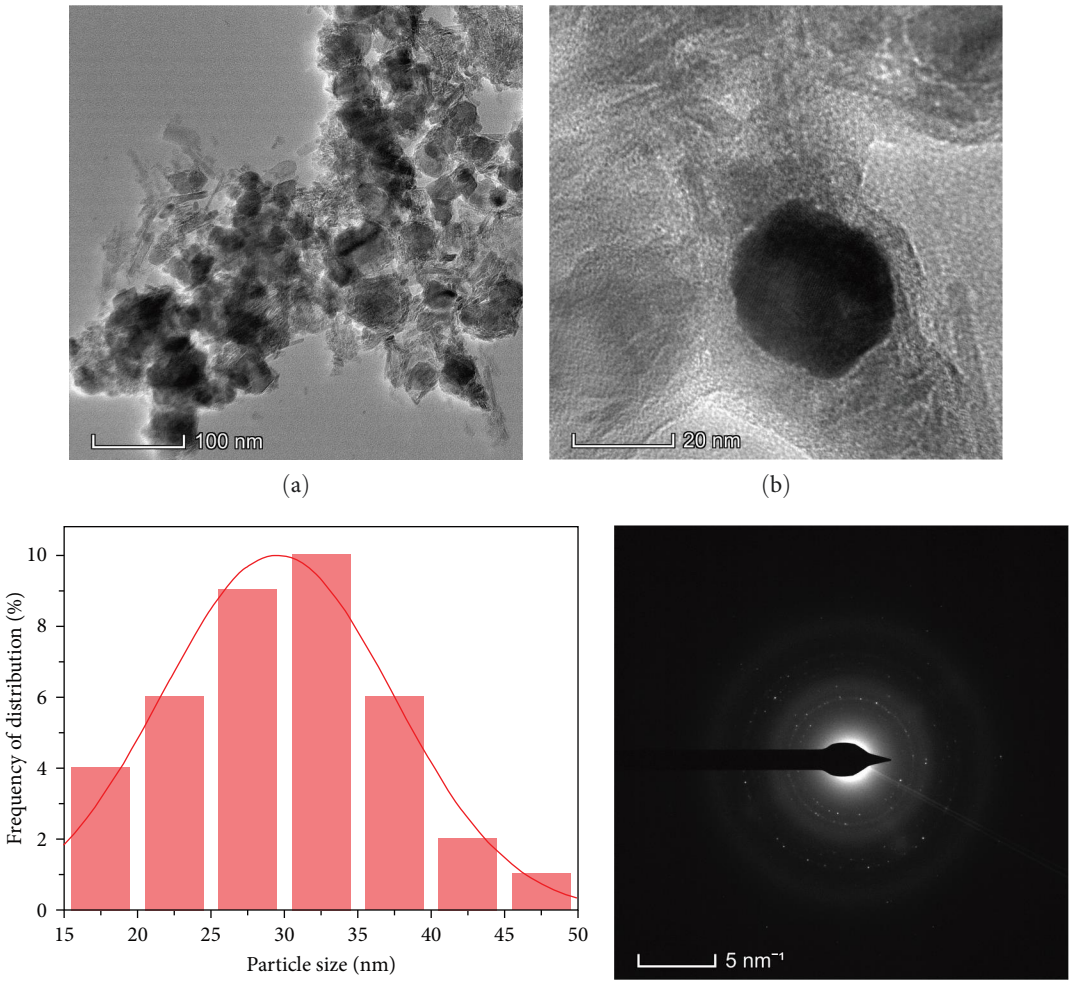

Figure 3: (a) TEM image of Fe_3O_4 nanoparticles, (b) HRTEM image of Fe_3O_4 nanoparticles, (c) size distribution of Fe_3O_4 nanoparticles, and (d) SAED pattern of Fe_3O_4 nanoparticles.

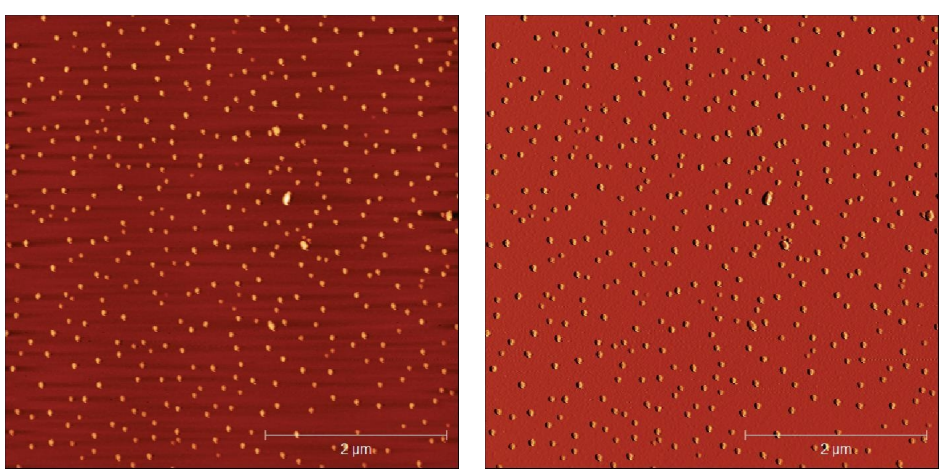

Figure 4: Continued.

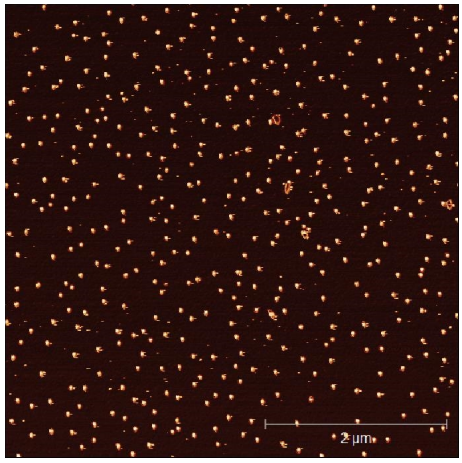

(c)

Figure 4: (a) AFM image (topography) of Fe_3O_4 nanoparticles, (b) AFM image (amplitude) of Fe_3O_4 nanoparticles, and (c) AFM image (phase) of Fe_3O_4 nanoparticles.

Table 2: Particles size and surface roughness of Fe_3O_4 nanoparticles.

Average particle size (nm)	RMS roughness (nm)	Grain-wise RMS (nm)	Mean roughness (nm)	Skewness
58.043	20.6954	20.6954	11.4536	3.43140

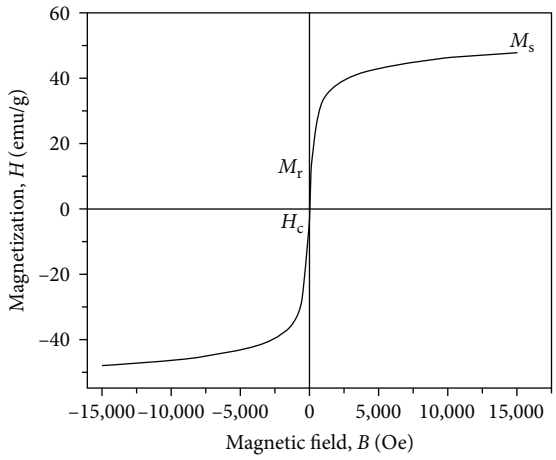

Figure 5: B–H (hysteresis) curve of Fe_3O_4 nanoparticles.

Table 3: Magnetic properties of Fe_3O_4 nanoparticles.

Saturation magnetization (emu/g)	Remnant magnetization (emu/g)	Coercivity (Oe)
50.75	3.03	30.09

magnetite particles may affect the value of saturation magnetization as a contribution from surface anisotropy. Since all the produced samples are virtually spherical, surface anisotropy should be expected to have little effect. The inadequate crystallization of magnetite during reaction synthesis may be the cause of a further drop in M_s. Changes in the population of the A and B sites may also contribute to the decline in saturation magnetization [40–42].

A long-range magnetic dipole–dipole interaction between the assemblies of superparamagnetic nanoparticles is not present, as shown by the disappearance of hysteresis at a small retentivity of 3.03 emu/g and coercivity (H_c) of 30.09 Oe (Figure 5). This

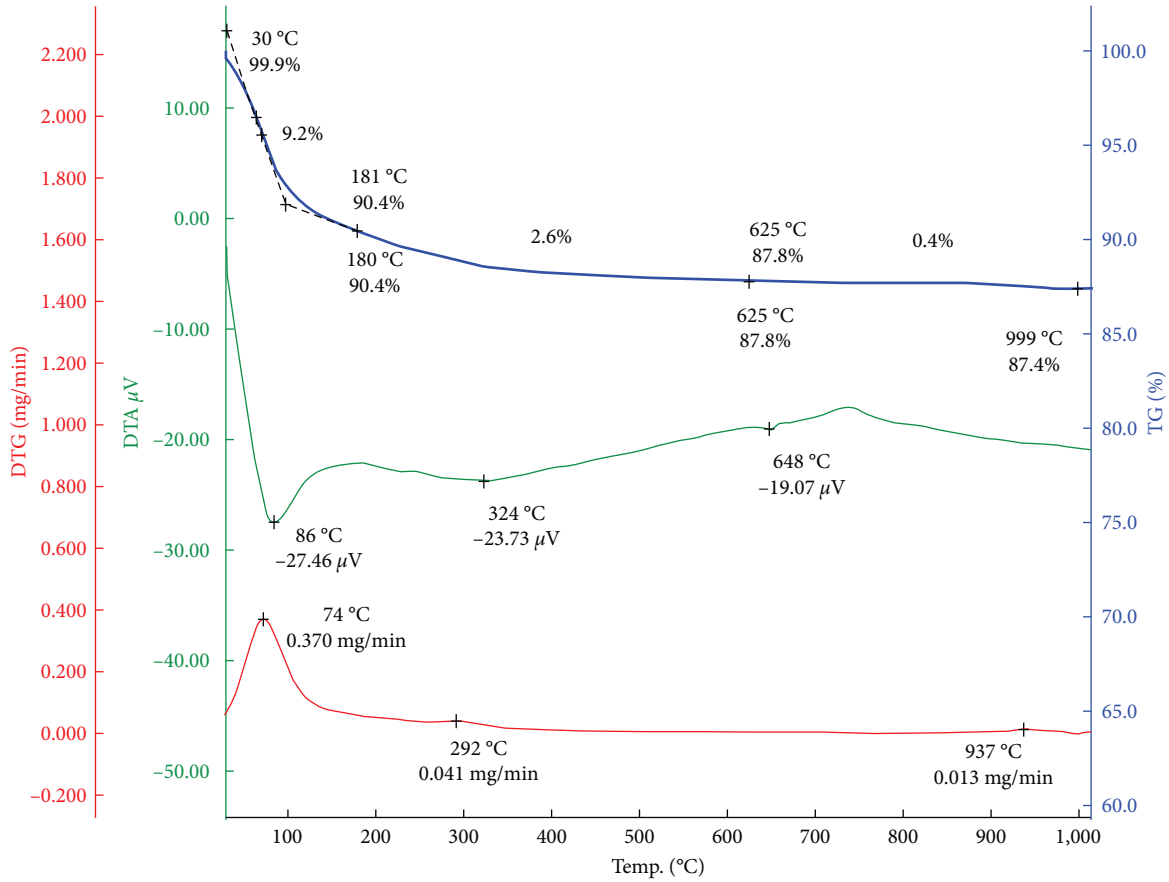

Figure 6: TG-DTA curve of Fe_3O_4 nanoparticles.

indicates that when exposed to a magnetic field, the produced magnetite quickly demonstrated magnetization.

3.6. TG-DTA. The produced Fe_3O_4 nanoparticles were subjected to synchronized thermogravimetric and differential TG-DTA, which was carried out in a nitrogen atmosphere with an increment of 20°C/min and temperatures ranging from 25 to 1,000°C. Three predictable weight losses have been identified, according to the TG graph (Figure 6). The temperature between 30 and 180°C causes a major weight loss of about 9.2%, which is caused by the evaporation of absorbed water. The second weight loss is caused by the degradation of unrefined material, e.g., NaOH and occurs in the temperature range of 180–625°C. The third weight loss confirms the formation of corresponding metal oxide and the spinel phase. There is no weight loss above 625°C, i.e., TGA curves remain steady, which indicates the absolute volatility of water, the completion of the crystallization route, and the immediate formation of pure materials. DTG curve (Figure 6) shows that the decomposition of absorbed water molecules occurs at 86°C, where the maximum decomposition rate is about 0.37 mg/min. The DTA curve generally shows that the prepared materials undergo both exothermic and endothermic reactions. The DTA curve (Figure 6) revealed that three endothermic peaks occur at 86°C due to dehydration and 324 and 618°C due to the decomposition of anhydrous precursor, respectively [43].

4. Conclusion

The chemical production of magnetite nanoparticles was carried out by a simple and facile coprecipitation in an aqueous solution using iron salt as a precursor. TEM image shows that the synthesized magnetite nanoparticles have a spherical particle form with an average diameter of about 30 nm, while SEM and AFM image shows bigger particle sizes because particles agglomerated due to calcination at 250°C for 4 hr. The iron oxide crystal phase could be face-centered cubic magnetite (Fe_3O_4), according to XRD results. Because there was little coercitivity for the hysteresis cycles, measurements of magnetization as a function of the field revealed superparamagnetism behavior in the material. The average diameter of synthesized magnetite nanoparticles proved to be perfect for applications in drug delivery, MRI contrast agents, catalysis, degradation of antibiotics, antibacterial activity, removal of heavy metals and organic dyes, etc.

Data Availability

The data used to support the findings of this study are included in the article.

Conflicts of Interest

The authors affirm that they have no known financial or interpersonal conflicts that would have appeared to have an impact on the research presented in this study.

Acknowledgments

The authors appreciate the technical assistance provided by Pilot Plant and Process Development Center. Additionally, the technical assistance of Mr. Md. Shofiqul Islam and Mrs. Monira Binte Mesbah, Scientific Officers of Pilot Plant and Process Development Center are sincerely acknowledged by the authors.

References

[1] P. Fraga-García, P. Kubbutat, M. Brammen, S. Schwaminger, and S. Berensmeier, "Bare iron oxide nanoparticles for magnetic harvesting of microalgae: from interaction behavior to process realization," *Nanomaterials (Basel, Switzerland)*, vol. 8, no. 5, 2018.

[2] J. Yuan, Y. Chen, H. Li et al., "New insights into the cellular responses to iron nanoparticles in *Capsicum annuum*," *Scientific Reports*, vol. 8, no. 1, pp. 1–9, 2018.

[3] W. H. Elmer and J. C. White, "The use of metallic oxide nanoparticles to enhance growth of tomatoes and eggplants in disease infested soil or soilless medium," *Environmental Science: Nano*, vol. 3, no. 5, pp. 1072–1079, 2016.

[4] P. Xu, G. M. Zeng, D. L. Huang et al., "Use of iron oxide nanomaterials in wastewater treatment: a review," *Science of The Total Environment*, vol. 424, pp. 1–10, 2012.

[5] N. A. Krans, E. C. van der Feltz, J. Xie, I. A. Dugulan, J. Zečević, and K. P. de Jong, "Attachment of iron oxide nanoparticles to carbon nanotubes and the consequences for catalysis," *ChemCatChem*, vol. 10, no. 16, pp. 3388–3391, 2018.

[6] J. Lin, A.-Rahman O. Raji, K. Nan et al., "Iron oxide nanoparticle and graphene nanoribbon composite as an anode material for high-performance li-ion batteries," *Advanced Functional Materials*, vol. 24, no. 14, pp. 2044–2048, 2014.

[7] H. Yuan, M. Q. Wilks, M. D. Normandin, G. El Fakhri, C. Kaittanis, and L. Josephson, "Heat-induced radiolabeling and fluorescence labeling of Feraheme nanoparticles for PET/SPECT imaging and flow cytometry," *Nature Protocols*, vol. 13, no. 2, pp. 392–412, 2018.

[8] K. Hola, Z. Markova, G. Zoppellaro, J. Tucek, and R. Zboril, "Tailored functionalization of iron oxide nanoparticles for MRI, drug delivery, magnetic separation and immobilization of biosubstances," *Biotechnology Advances*, vol. 33, no. 6, pp. 1162–1176, 2015.

[9] D. Ling, N. Lee, and T. Hyeon, "Chemical synthesis and assembly of uniformly sized iron oxide nanoparticles for medical applications," *Accounts of Chemical Research*, vol. 48, no. 5, pp. 1276–1285, 2015.

[10] S. Laurent, A. A. Saei, S. Behzadi, A. Panahifar, and M. Mahmoudi, "Superparamagnetic iron oxide nanoparticles for delivery of therapeutic agents: opportunities and challenges," *Expert Opinion on Drug Delivery*, vol. 11, no. 9, pp. 1449–1470, 2014.

[11] C. Martinez-Boubeta, K. Simeonidis, A. Makridis et al., "Learning from nature to improve the heat generation of iron-oxide nanoparticles for magnetic hyperthermia applications," *Scientific Reports*, vol. 3, Article ID 1652, 2013.

[12] A. F. Alves, S. G. Mendo, L. P. Ferreira et al., "Gelatine-assisted synthesis of magnetite nanoparticles for magnetic hyperthermia," *Journal of Nanoparticle Research*, vol. 18, Article ID 27, 2016.

[13] Y. Bao, J. A. Sherwood, and Z. Sun, "Magnetic iron oxide nanoparticles as T_1 contrast agents for magnetic resonance imaging," *Journal of Materials Chemistry C*, vol. 6, no. 6, pp. 1280–1290, 2018.

[14] R. Hachani, M. Lowdell, M. Birchall et al., "Polyol synthesis, functionalisation, and biocompatibility studies of superparamagnetic iron oxide nanoparticles as potential MRI contrast agents," *Nanoscale*, vol. 8, no. 6, pp. 3278–3287, 2016.

[15] S. Laurent, D. Forge, M. Port et al., "Magnetic iron oxide nanoparticles: synthesis, stabilization, vectorization, physicochemical characterizations and biological applications," *Chemical Reviews*, vol. 108, no. 6, pp. 2064–2110, 2008.

[16] M. O. Besenhard, A. P. LaGrow, A. Hodzic et al., "Co-precipitation synthesis of stable iron oxide nanoparticles with NaOH: new insights and continuous production via flow chemistry," *Chemical Engineering Journal*, vol. 399, Article ID 125740, 2020.

[17] X. Sun, C. Zheng, F. Zhang et al., "Size-controlled synthesis of magnetite (Fe_3O_4) nanoparticles coated with glucose and gluconic acid from a single Fe(III) precursor by a sucrose bifunctional hydrothermal method," *The Journal of Physical Chemistry C*, vol. 113, no. 36, pp. 16002–16008, 2009.

[18] C.-J. Chen, H.-Y. Lai, C.-C. Lin, J.-S. Wang, and R.-K. Chiang, "Preparation of monodisperse iron oxide nanoparticles via the synthesis and decomposition of iron fatty acid complexes," *Nanoscale Research Letters*, vol. 4, no. 11, pp. 1343–1350, 2009.

[19] T. Hyeon, Y. Chung, J. Park, S. S. Lee, Y.-W. Kim, and B. H. Park, "Synthesis of highly crystalline and monodisperse cobalt ferrite nanocrystals," *The Journal of Physical Chemistry B*, vol. 106, no. 27, pp. 6831–6833, 2002.

[20] B. H. Kim, N. Lee, H. Kim et al., "Large-scale synthesis of uniform and extremely small-sized iron oxide nanoparticles for high-resolution T_1 magnetic resonance imaging contrast agents," *Journal of the American Chemical Society*, vol. 133, no. 32, pp. 12624–12631, 2011.

[21] S. G. Kwon, Y. Piao, J. Park et al., "Kinetics of monodisperse iron oxide nanocrystal formation by "heating-up" process," *Journal of the American Chemical Society*, vol. 129, no. 41, pp. 12571–12584, 2007.

[22] A. Lassenberger, T. A. Grünewald, P. D. J. van Oostrum et al., "Monodisperse iron oxide nanoparticles by thermal decomposition: elucidating particle formation by second-resolved in situ small-angle X-ray scattering," *Chemistry of Materials*, vol. 29, no. 10, pp. 4511–4522, 2017.

[23] I.-M. Grabs, C. Bradtmöller, D. Menzel, and G. Garnweitner, "Formation mechanisms of iron oxide nanoparticles in different nonaqueous media," *Crystal Growth & Design*, vol. 12, no. 3, pp. 1469–1475, 2012.

[24] W. Wu, C. Z. Jiang, and V. A. L. Roy, "Designed synthesis and surface engineering strategies of magnetic iron oxide nanoparticles for biomedical applications," *Nanoscale*, vol. 8, no. 47, pp. 19421–19474, 2016.

[25] M. K. Lima-Tenório, E. A. G. Pineda, N. M. Ahmad, H. Fessi, and A. Elaissari, "Magnetic nanoparticles: in vivo cancer diagnosis and therapy," *International Journal of Pharmaceutics*, vol. 493, no. 1-2, pp. 313–327, 2015.

[26] T. Ahn, J. H. Kim, H.-M. Yang, J. W. Lee, and J.-D. Kim, "Formation pathways of magnetite nanoparticles by coprecipitation method," *The Journal of Physical Chemistry C*, vol. 116, no. 10, pp. 6069–6076, 2012.

[27] J. Baumgartner, A. Dey, P. H. H. Bomans et al., "Nucleation and growth of magnetite from solution," *Nature Materials*, vol. 12, no. 4, pp. 310–314, 2013.

[28] J.-P. Jolivet, C. Chanéac, and E. Tronc, "Iron oxide chemistry. From molecular clusters to extended solid networks," *Chemical Communications*, vol. 4, no. 5, pp. 481–483, 2004.

[29] S. Sun, D. Gebauer, and H. Cölfen, "Alignment of amorphous iron oxide clusters: a non-classical mechanism for magnetite formation," *Angewandte Chemie International Edition*, vol. 56, no. 14, pp. 4042–4046, 2017.

[30] M. B. Andrade, T. R. T. Santos, M. F. Silva, M. F. Vieira, R. Bergamasco, and S. Hamoudi, "Graphene oxide impregnated with iron oxide nanoparticles for the removal of atrazine from the aqueous medium," *Separation Science and Technology*, vol. 54, no. 16, pp. 2653–2670, 2019.

[31] D. M. Fernandes, J. L. Andrade, M. K. Lima et al., "Thermal and photochemical effects on the structure, morphology, thermal and optical properties of PVA/Ni0.04Zn0.96O and PVA/Fe 0.03Zn0.97O nanocomposite films," *Polymer Degradation and Stability*, vol. 98, no. 9, pp. 1862–1868, 2013.

[32] S. Atiq, M. Javid, S. Riaz, and S. Naseem, "Magnetic phase transition in nickel oxide," *Materials Today: Proceedings*, vol. 2, Part B, no. 10, pp. 5262–5267, 2015.

[33] Q. Li, C. W. Kartikowati, S. Horie, T. Ogi, T. Iwaki, and K. Okuyama, "Correlation between particle size/domain structure and magnetic properties of highly crystalline F_e3O_4 nanoparticles," *Scientific Reports*, vol. 7, no. 1, pp. 1–4, 2017.

[34] S. S. Alterary and A. Alkhamees, "Synthesis, surface modification, and characterization of Fe_3O_4@SiO_2core@shell nanostructure," *Green Processing and Synthesis*, vol. 10, no. 1, pp. 384–391, 2021.

[35] G. Predoi, C. S. Ciobanu, S. L. Iconaru et al., "Preparation and characterization of dextran coated iron oxide nanoparticles thin layers," *Polymers*, vol. 13, no. 14, Article ID 2351, 2021.

[36] G. F. Goya, T. S. Berquó, F. C. Fonseca, and M. P. Morales, "Static and dynamic magnetic properties of spherical magnetite nanoparticles," *Journal of Applied Physics*, vol. 94, no. 5, pp. 3520–3528, 2003.

[37] B. Wang, Q. Wei, and S. Qu, "Synthesis and characterization of uniform and crystalline magnetite nanoparticles via oxidation–precipitation and modified co-precipitation methods," *International Journal of Electrochemical Science*, vol. 8, no. 3, pp. 3786–3793, 2013.

[38] N. Mahmed, O. Heczko, O. Söderberg, and S. P. Hannula, "Room temperature synthesis of magnetite ($Fe_{3-\delta}O_4$) nanoparticles by a simple reverse co-precipitation method," *IOP Conference Series: Materials Science and Engineering*, vol. 18, Article ID 032020, 2011.

[39] R. M. Cornell and U. Schwertmann, "The iron oxides: structure, properties, reactions, ocurrences and uses," in *Transformations*, pp. 365–407, Wiley, 2003.

[40] M. P. Morales, M. Andres-Vergés, S. Veintemillas-Verdaguer, M. I. Montero, and C. J. Serna, "Structural effects on the magnetic properties of γ-Fe_2O_3 nanoparticles," *Journal of Magnetism and Magnetic Materials*, vol. 203, no. 1–3, pp. 146–148, 1999.

[41] F. Bødker, S. Mørup, and S. Linderoth, "Surface effects in metallic iron nanoparticles," *Physical Review Letters*, vol. 72, no. 2, pp. 282–285, 1994.

[42] G. F. Goya, "Magnetic dynamics of $Zn57Fe_2O_4$ nanoparticles dispersed in a ZnO matrix," *IEEE Transactions on Magnetics*, vol. 38, no. 5, pp. 2610–2612, 2002.

[43] E. Catalano and A. Di Benedetto, "Characterization of physicochemical and colloidal properties of hydrogel chitosan-coated iron-oxide nanoparticles for cancer therapy," *Journal of Physics: Conference Series*, vol. 841, Article ID 012010, 2017.